Bull Volcanol (1999) 61:1–14 

ORIGINAL PAPER

**S. K. Rowland · M. E. MacKay · H. Garbeil**
**P. J. Mouginis-Mark**

# Topographic analyses of Kīlauea Volcano, Hawai'i, from interferometric airborne radar

Received: 28 April 1998 / Accepted: 1 February 1999

**Abstract** We analyze digital topographic data collected in September 1993 over a ~500-km$^2$ portion of Kīlauea Volcano, Hawai'i, by the C-band (5.6-cm wavelength) topographic synthetic aperture radar (TOPSAR) airborne interferometric radar. Field surveys covering an ~1-km$^2$ area of the summit caldera and the distal end of an ~8-m-thick 'a'ā flow indicate that the 10-m spatial resolution TOPSAR data have a vertical accuracy of 1–2 m over a variety of volcanic surfaces. After conversion to a common datum, TOPSAR data agree favorably with a digital elevation model (DEM) produced by the U.S. Geological Survey (USGS), with the important exception of the region of the ongoing eruption (which postdates the USGS DEM). This DEM comparison gives us confidence that subtracting the USGS data from TOPSAR data will produce a reasonable estimate of the erupted volume as of September 1993. This subtraction produces dense rock equivalent (DRE) volumes of 392, 439, and $90 \times 10^6$ m$^3$ for the Pu'u 'Ō'ō, Kūpa'ianahā, and episode 50–53 stages of the eruption, respectively. These are 124, 89, and 94% of the volumes calculated by staff of the Hawaiian Volcano Observatory (HVO) but do not include lava of Kūpa'ianahā and episodes 50–53 that flowed into the ocean and are thus invisible to TOPSAR. Accounting for this lava increases the TOPSAR volumes to 124, 159, and 129% of the HVO volumes. Including the ±2-m uncertainty derived from the field surveys produces TOPSAR-derived volumes for the eruption as a whole that range between 81 and 125% of the USGS-derived values. The vesicularity- and ocean-corrected TOPSAR volumes yield volumetric eruption rates of 4.5, 4.5, and 2.7 m$^3$/s for the three stages of the eruption, which compare with HVO-derived values of 3.6, 2.8, and 2.1 m$^3$/s, respectively. Our analysis shows that care must be taken when vertically registering the TOPSAR and USGS DEMs to a common datum because C-band TOPSAR penetrates only partially into thick forest and therefore produces a DEM within the tree canopy, whereas the USGS DEM is adjusted for vegetation.

**Key words** Digital elevation model · TOPSAR · Interferometry · Eruption volume · Digital topography

Editorial responsibility: D. A. Swanson

Scott K. Rowland (✉) · Mary E. MacKay · Harold Garbeil
Peter J. Mouginis-Mark
Hawai'i Institute of Geophysics and Planetology, University of Hawai'i at Mānoa, 2525 Correa Road, Honolulu, Hawai'i 96822, USA, and Hawai'i Center for Volcanology
e-mail: scott@pgd.hawaii.edu

## Introduction

Understanding the morphology and long-term volumetric output of a volcano is valuable for constraining magma supply as well as providing information about magma plumbing systems and long-term eruptive cycles (e.g., Wadge 1977; Crisp 1984; Holcomb 1987; Moore and Mark 1992; Dvorak and Dzurisin 1993). Until recently, most flow-volume estimates have relied on measuring flow margin thicknesses at multiple locations and multiplying these by planimetric flow areas, or by time-consuming surveying campaigns (e.g., Fink and Zimbelman 1990; Stevens et al. 1997). Unless knowledge is available about the pre-flow topography (Stevens et al. 1997), flow thicknesses away from flow margins must be estimated. When sufficiently accurate measurements of individual flow volumes and morphologies are available, information may also be gained about the rheological properties of the flows (e.g., Hulme 1974; Fink and Zimbelman 1990). New airborne and spaceborne radar techniques offer a powerful remote sensing approach to address these flow volume and morphology problems, provided that the accuracy and limitations of the technique are considered.

Interferometric radar such as topographic synthetic aperture radar (TOPSAR; Zebker et al. 1992) and the closely related technique of repeat-pass radar interfe-

rometry (Gabriel et al. 1989; Zebker et al. 1994a) hold the promise of producing detailed topographic maps over large areas of the world, many of which have never been accurately surveyed (Zebker et al. 1994b). Because these techniques determine an elevation at each picture element (pixel) in a scene, the digital elevation model (DEM) thus produced has a strong advantage over a DEM produced by interpolating between contour lines or spot elevations. The nominally high spatial resolution of the interferometric technique (10 m horizontally and 1–2 m vertically in the case of TOPSAR) permits improved quantitative investigation of volcanic geomorphology. Additionally, because of radar's ability to penetrate cloud cover, interferometric DEMs can be produced where cloud-free air photos (from which contour maps are derived) are difficult to collect.

Several volcanologic studies have been undertaken using data derived from the TOPSAR instrument. These include studies of lava flows and a moberg ridge at Hekla, Iceland (Evans et al. 1992), valleys and potential flow paths at Vesuvius, Italy (Mouginis-Mark and Garbeil 1993), and the slopes and lava flow volumes on Galápagos volcanoes (Rowland 1996; Mouginis-Mark et al. 1996). Additional analyses will undoubtedly be based on TOPSAR data for different volcanoes; the Fall 1996 PacRim deployment of TOPSAR collected topographic data for several volcanoes in the western Pacific, including Taal, Pinatubo, and Canlaon in the Philippines, White Island and Ruapehu in New Zealand, and Mauna Loa and East Maui Volcano in Hawai'i.

As the number of these studies increases, however, it becomes important to understand the accuracy and limitations of the data for different geographic settings and volcanic surfaces. We investigated the relative accuracy of TOPSAR measurements within a scene (as opposed to the absolute accuracy of the whole scene), using both field measurements and comparison with a U.S. Geological Survey (USGS) DEM derived by stereogrammetry. Key uncertainties with the TOPSAR data are the relative vertical accuracy of height values within a scene (e.g., across flow margins and fault scarps) and the representation of topography over surfaces that are highly variable on a sub-pixel scale (e.g., extremely rough flows). Several studies of TOPSAR accuracy have been performed in non-volcanic areas (e.g., Lin et al. 1994); notably, Izenberg et al. (1996) used field transits and an electronic distance meter (EDM) to validate TOPSAR data for a flood plain along the Missouri River. This flood plain was very flat, however, and had very different micro-topographic characteristics from those of basaltic lava flows.

We focus on TOPSAR data collected on 30 September 1993, over Kīlauea Volcano, Hawai'i (Fig. 1). These data have a spatial resolution of 10 m/pixel and cover a swath that is 40 km long by approximately 12.8 km wide. Our study areas include the summit caldera and flows and vents of the ongoing Pu'u 'Ō'ō/Kūpa'ianahā eruption. We first investigate the accuracy of the TOPSAR data by comparing the TOPSAR DEM with field data collected with a total field station (TFS) in the southwestern part of the caldera and on the distal end of a 1985 Pu'u 'Ō'ō flow near the coast (Fig. 1). We then use a pre-eruption USGS DEM and the TOPSAR data to estimate the volume of material erupted from January 1983 to September 1993, and in turn to estimate average effusion rates during this interval. Volumes and effusion rates were calculated by the staff of the Hawaiian Volcano Observatory (HVO) and thus provide an excellent data set against which we can assess TOPSAR accuracy. In addition to the field checking and DEM comparisons, we utilized Landsat Thematic Mapper (TM) data to investigate how vegetation affects TOPSAR accuracy.

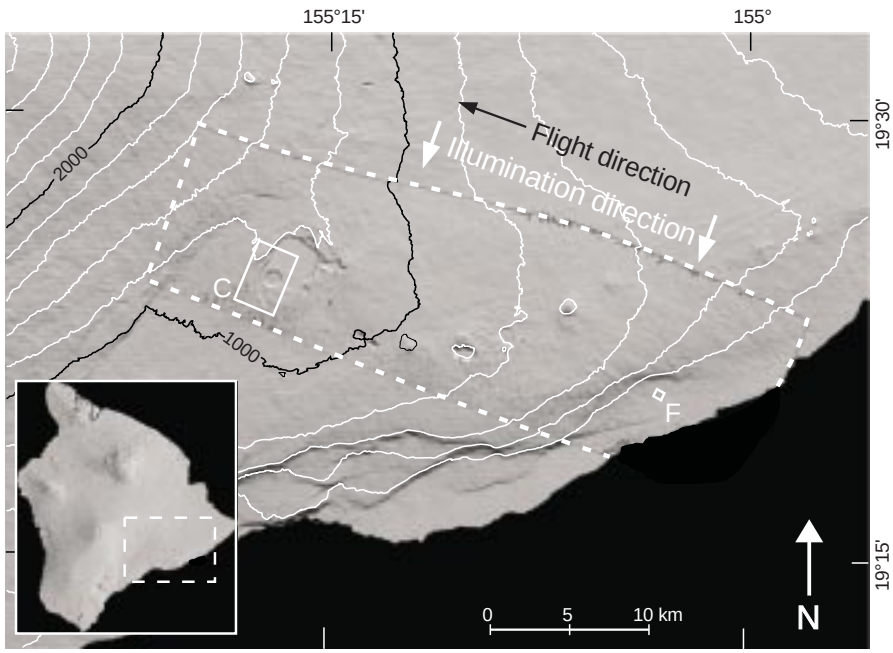


**Fig. 1** Shaded-relief image shows the location of the topographic synthetic aperture radar (TOPSAR) swath used in this study. TOPSAR data were superimposed on the U.S. Geological Survey digital elevation model (USGS DEM), with a contour interval of 200 m. The TOPSAR flight azimuth was 291° with a radar illumination azimuth of 201°. *Dashed line* outlines TOPSAR data swath (and area of Fig. 6). *Boxes* indicate locations of summit caldera study area (*C*; see Figs. 2A, 3) and 1985 flow study area (*F*; see Fig. 4). *Dashed box* in *inset* shows location of larger map

### Radar and interferometry

Numerous texts deal in detail with the physics and theory of synthetic aperture radar (SAR) imaging systems (e.g., Elachi 1988). Two or more SAR images can be combined interferometrically to derive topography (Zebker and Goldstein 1986). Interferometric radars such as TOPSAR (Zebker et al. 1992; Madsen et al. 1995), use two antennae on the same platform with an accurately known baseline separation. Radar interferometry is similar but uses platforms with single antennae to collect the two images and thus requires two closely spaced, parallel orbits or flights (e.g., Gabriel et al. 1989; Massonnet et al. 1993; Zebker et al. 1994a). The processing of interferometric radar data to produce topographic information is complex, and we summarize the basic principles in Appendix 1.

TOPSAR is flown on the NASA DC-8 research aircraft (Zebker et al. 1992). The data for this study were collected using two C-band (5.6-cm wavelength) antennae mounted on the left side of the plane, with a 2.6-m-long baseline between them. The aircraft flies at an altitude of 26,000 feet (~7930 m), producing incidence angles from ~7° in the near range to ~60° in the far range.

## TOPSAR comparison with ground data

To characterize the local accuracy of the TOPSAR DEM (i.e., on the scale of geological features such as fault scarps or single lava flows), we conducted ground surveys with a TFS (Wild Heerbrugg Ltd., Switzerland), consisting of a Wild Theomat T3000 theodolite fitted with a DI2000 EDM. The corner reflectors were mounted on 1.4-m-high staffs and held by hand. The TFS data were automatically stored in a record module and later downloaded to a portable computer. Corner-reflector points in each survey area were collected as horizontal angle (with respect to a zero line of known azimuth), vertical angle (with respect to horizontal), and distance. These data were converted to x, y, and z values using spreadsheet software and a GPS-derived base station location. We estimate that these values are accurate relative to each other to ±5 cm. We created a DEM by interpolating between the individual x–y–z points using the Geographic Mapping Tool package (GMT; Wessel and Smith 1995) and generated a shaded-relief image to facilitate coregistration with TOPSAR data. This TFS DEM was gridded at a 5-m spacing, necessitating a resampling of the TOPSAR DEM from 10 to 5 m for coregistration.

### Kīlauea Caldera ground truth

We completed a survey of ~800 points spaced 10–20 m apart within the southwest part of Kīlauea caldera (Figs. 1, 2A). Here the caldera margin consists of multiple downdropped fault blocks, and the caldera floor slopes gently away from the rim of Halema‘uma‘u pit crater. The instrument site was located on the edge of one of the fault blocks, which allowed data to be collected along the outermost caldera rim, on several of the smaller fault blocks, and on a portion of the caldera floor.

Figure 2A presents the difference between the TOPSAR and TFS DEMs. Most of the image shows differences between –3 and +3 m, with the largest differences occurring at the tops and bottoms of caldera faults (see below). Figure 3C compares the two data sets only at TFS corner-reflector sites. When the two groups of outlier points (1 and 2; see below) are not included, the data fall on a best-fit line with a correlation coefficient of 0.99, indicating excellent agreement over the survey area. The RMS error (after removal of a 7.85-m mean offset) is 2.14 m. The slope of the best-fit line is 0.94 (i.e., rotated slightly clockwise from a slope of 1), meaning that relative to the TFS elevations higher-elevation points in the TOPSAR data are slightly too low and/or lower-elevation points are slightly too high. In this field area the lower elevations are to the north and the higher elevations to the south; additionally, north and south correspond to near-range and far-range in the radar swath. The best-fit slope may therefore indicate a slight downrange tilt in the TOPSAR data, equivalent to ~10 m across 2.25 km of swath, or 0.25°.

Two groups of outliers (1 and 2 in Fig. 3; defined by being outside two standard deviations) correspond to large differences in Fig. 2A, and result from the inability to exactly register the two DEMs as well as from safety considerations during the field survey. Cluster 1 represents TFS points on the main caldera floor at the base of a large scarp. Although misregistration is only slight, it has aligned these points with the top of the scarp in the TOPSAR data. In a similar study Madsen et al. (1995) reported that misregistration equivalent to as little as 2.5 m increased vertical differences by 15–25%. Cluster 2 corresponds to the top of a scarp where hazardous conditions prevented setting up the corner reflectors close to the edge. The resulting scarp in the TFS data is therefore shifted from its actual location. Finally, even where registration is nearly exact, the interpolation of TFS data to produce a continuous DEM rounded the sharp discontinuities (as illustrated in Fig. 3D), producing the positive errors at the tops of scarps in Fig. 2A.

### Flow margin ground truth

We also collected TFS data on the distal end of an ‘a‘ā flow erupted in 1985 from Pu‘u ‘Ō‘ō (Fig. 4A, B). Corner-reflector locations were 1–3 m apart, and we gridded the resulting DEM at a 1-m spacing; the TOPSAR DEM was resampled from 10 to 1 m for coregistration. The differences between field and TOPSAR elevations are small (Fig. 2B), although the outline of the

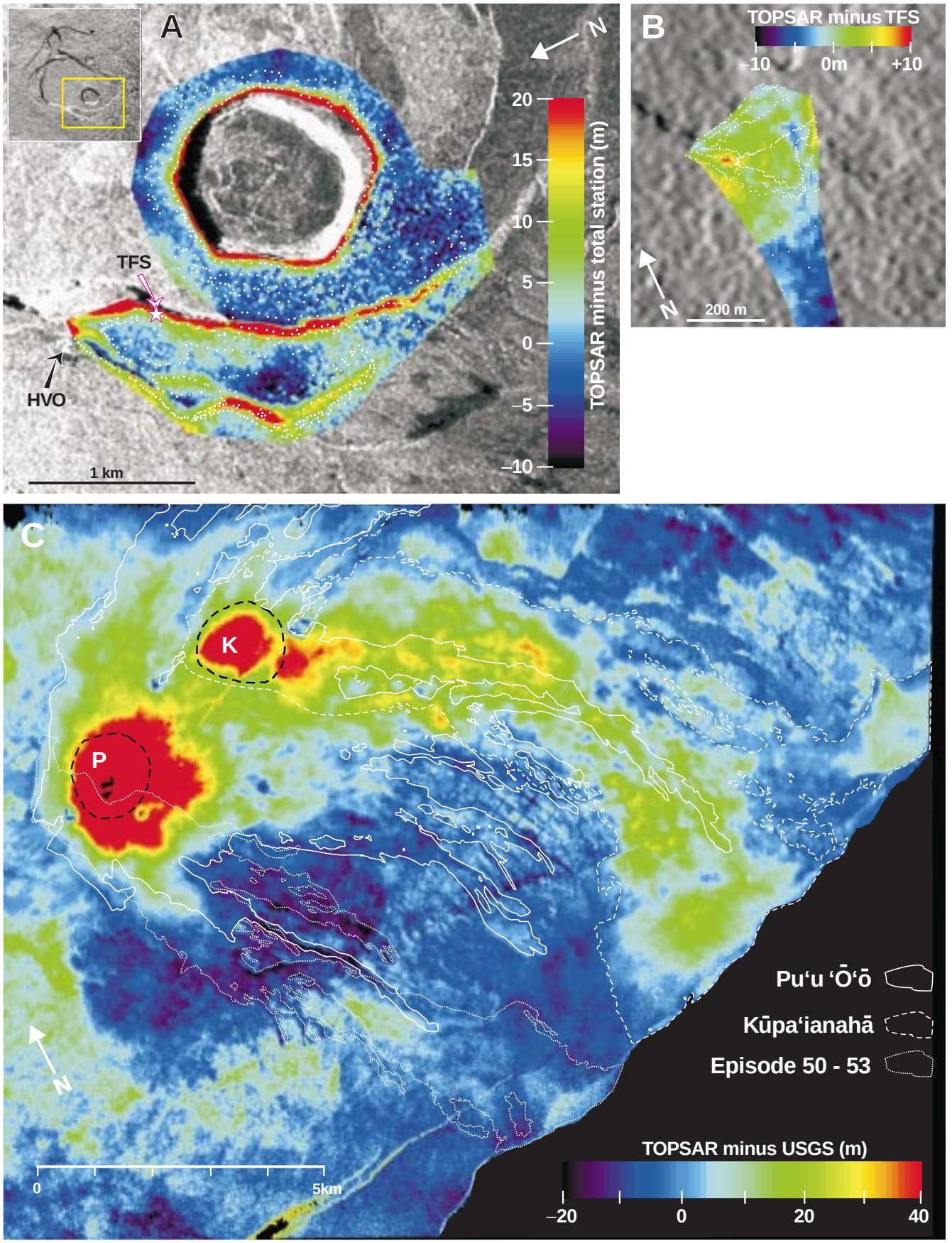
A
N
20
15
10
5
0
–5
–10
TOPSAR minus total station (m)
TFS
HVO
1 km
B
TOPSAR minus TFS
–10
0m
+10
N
200 m
C
K
P
N
0
5km
Puʻu ʻŌʻō
Kūpaʻianahā
Episode 50 - 53
TOPSAR minus USGS (m)
–20
0
20
40

**Fig. 2** **A** Elevation differences between TFS-derived elevations and TOPSAR for the southwest caldera study area (*C* in Fig. 1). Elevation differences indicated in *color*; radar backscatter makes up the remainder of the image. *White dots* indicate corner-reflector sites. *TFS* and *HVO* indicate total field station instrument site and Hawaiian Volcano Observatory, respectively. *Inset* (a shaded relief image) indicates location of study area (*yellow box*) with respect to the summit caldera. **B** Elevation differences between TOPSAR and TFS-derived elevations for the 1985 ʻaʻā flow study site (*F* in Fig. 1; see Fig. 5). Elevation differences indicated in *color*; shaded relief makes up the remainder of the image. *White dots* indicate corner-reflector locations. **C** Difference image created by subtracting the USGS DEM from the TOPSAR DEM and making a vertical correction of 75 m (see text). Flow fields of the current eruption are indicated as follows: *solid white* (Puʻu ʻŌʻō flows); *dashed black, P* (Puʻu ʻŌʻō cone); *dashed white* (Kūpaʻianahā flows); *dashed black, K* (Kūpaʻianahā shield); *dotted white* (episode 50–53 flows). Features of interest include a large ground crack between Puʻu ʻŌʻō and Kūpaʻianahā, and two old cinder cones now buried by Puʻu ʻŌʻō (south and west of the cone margin). The rectilinear pattern near the center of the image is produced by roads in the Royal Gardens subdivision (cut through vegetation); compare with labeled features in Fig. 8

flow can be discerned in the difference image, indicating slight misregistration. As with the caldera study, interpolation of the TFS data between reflector points accentuates areal errors. However, comparison of TOPSAR and uninterpolated TFS data at corner-reflector points along profiles over the flow show close agreement (Fig. 5). The RMS error for all points used in the profiles is 1.3 m, which is ~16% of the ~8-m flow thickness and on the order of the roughness of the flow surface (Fig. 4C).

We conclude from the field studies that within a scene TOPSAR data are accurate to within 1–2 m on typical basaltic surfaces. This holds for near-horizontal, mostly pāhoehoe flows and boulder-strewn ash such as occur in the caldera, as well as for extremely rough ʻaʻā surfaces such as those of the 1985 lava flow (Fig. 4C). TOPSAR is thus an excellent tool for determining morphologies, heights, and cross sections of lava flows, fault scarps, and vent structures, even when the surface roughness is considerable. We therefore infer that use-

**Fig. 3A–D** Comparisons of TOPSAR and TFS elevations at corner-reflector sites for the caldera study area. **A** Map showing corner-reflector sites, scarps, and the line of cross-section *x–x'*; *darker shading* surrounds groups of points 1 and 2 (discussed in text). **B** Shaded relief image indicating study area (*box*) with respect to caldera. **C** Graph of TOPSAR vs TFS elevations; *thick black line* is best-fit to data (excluding groups 1 and 2); comparison to slope of one indicated by *finest dashed line*. **D** Cross section over TOPSAR and TFS DEMs (*gray shading* and *dashed line*, respectively; no vertical exaggeration, elevation scale at left). *Thick solid line* shows TOPSAR minus TFS values (scale at right). Note how interpolative rounding of scarp edges in the TFS DEM produces large positive values

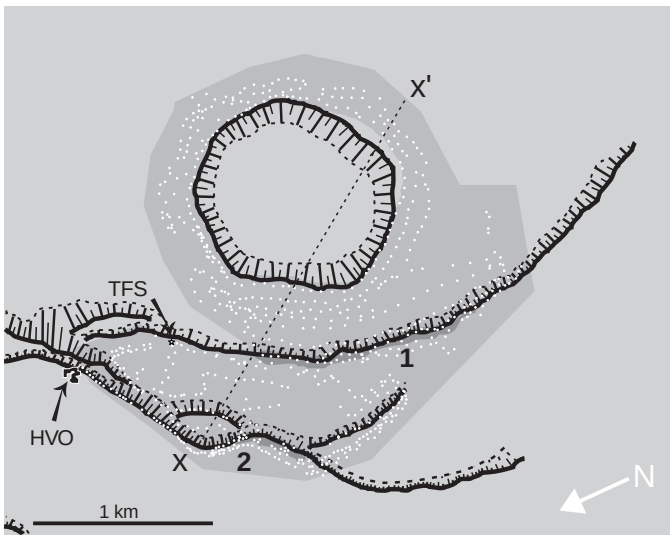


A

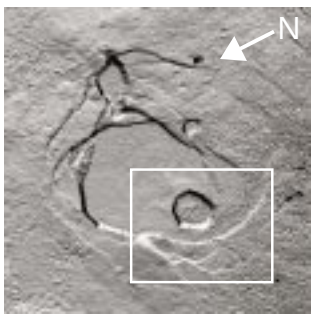


B

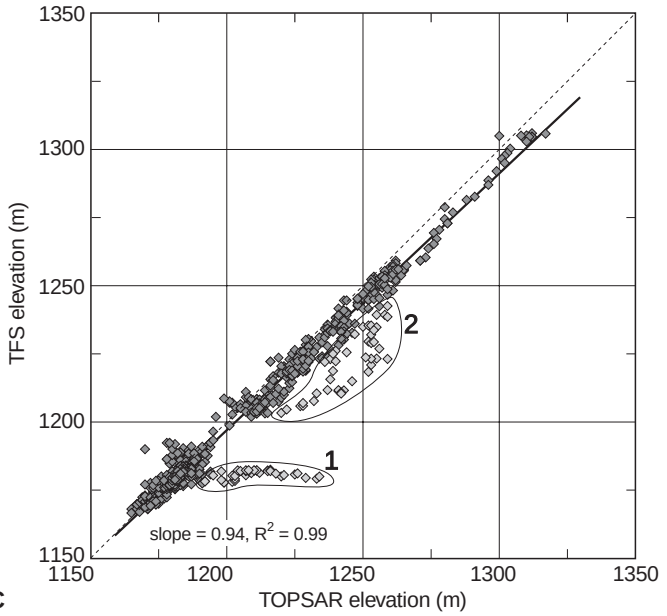


C

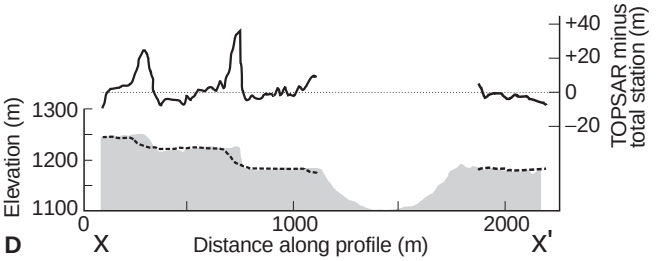


D

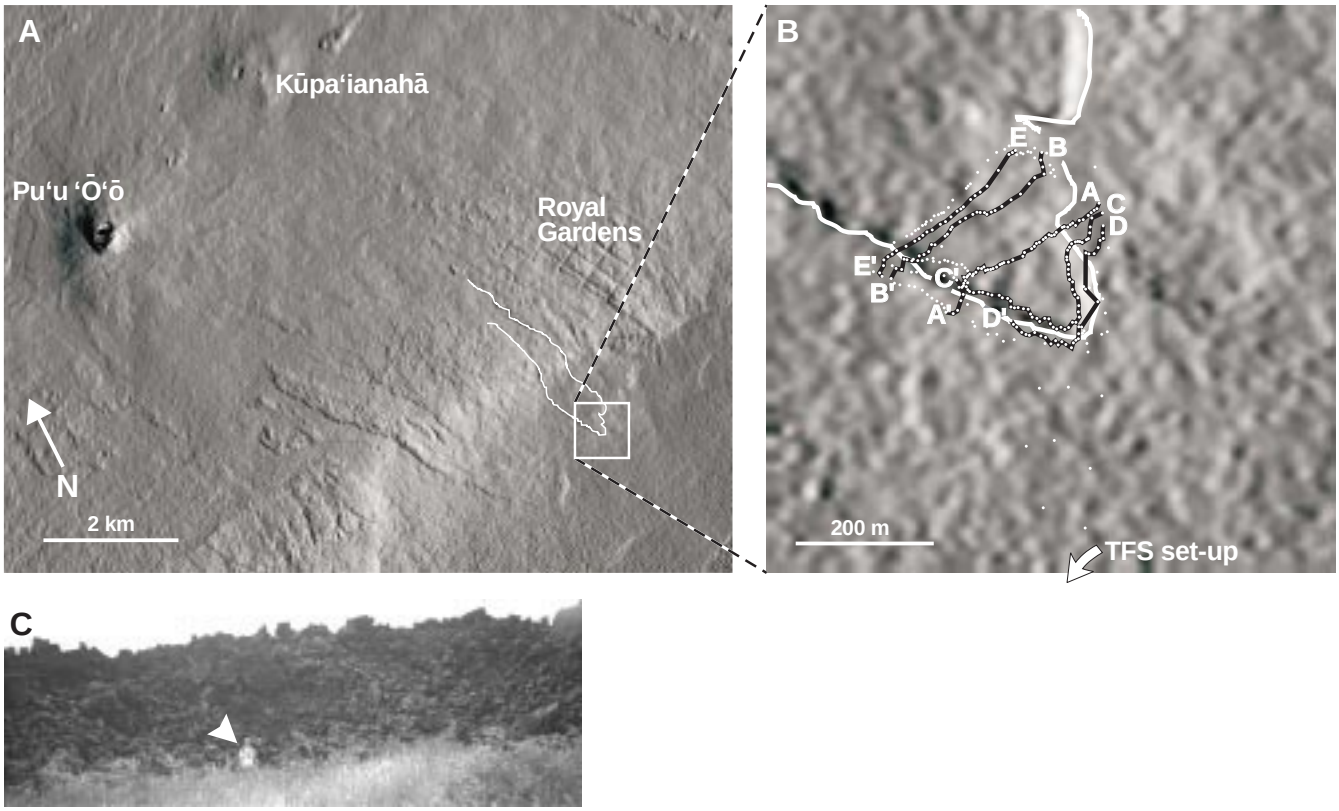


**Fig. 4A–C** The 1985 ʻaʻā flow study area. **A** Shaded relief of TOPSAR DEM giving an areal overview; *white line* indicates distal flow margin. **B** Shaded relief of distal portion of flow. *White line* indicates flow margin; *dots* indicate corner-reflector sites; *black lines* indicate paths of profiles shown in Fig. 5. **C** Photograph of the east margin of the flow, between profiles A and C. *Person* (*arrow*) indicates scale; note the roughness of the flow surface

ful lava flow parameters can be obtained from TOPSAR-derived topography (e.g., lava yield strengths from cross-sectional morphology or flow volumes from thickness measurements).

## Comparison of TOPSAR and USGS DEMS

As a second method of assessing relative TOPSAR accuracy, we compared the entire data swath with a mosaic of eight 7.5-min DEMs published by the USGS. Each 7.5-min DEM was produced by digitizing contour lines on topographic maps. Interpolation between the digitized contours produced a DEM gridded at a 10-m pixel spacing (e.g., USGS 1990; J. Kauahikaua, pers. commun.). These DEMs are available via the world wide web at: http://edcwww.cr.usgs.gov/Webglis/glisbin/search.pl?7_MIN_DEM

The contour data were derived from orthophotos created in 1977 and thus pre-date the Puʻu ʻŌʻō/Kūpaʻianahā eruption, which started 3 January 1983 (e.g., Wolfe et al. 1987, 1988).

We first coregistered the two data sets and produced a raw difference image by subtracting the USGS DEM from the TOPSAR DEM (Fig. 6A). A histogram of this image has a peak centered at +68 m, indicating an overall positive vertical offset in the TOPSAR data. Simple subtraction of 68 m from the difference image produces an image with many more near-zero values (Fig. 6B).

In the full-swath difference image (Fig. 6B), the flows and vents of the ongoing (January 1983 to present) eruption are the most obvious positive features because the USGS data pre-date the eruption. This suggests that the eruption volume can be determined from the difference image. Other features that stand out in the difference image correspond mainly to the steep walls of pit craters and the caldera. The walls facing away from the radar look-direction (i.e., facing southwest) cast radar shadows within which no TOPSAR data exist. The walls facing the radar (northeast) have been affected by layover (see Appendix 1) and are thus mislocated.

### DEM and vegetation corrections

The most obvious use of two DEMs created at different times during an eruption is to calculate the volume of new material by subtracting one DEM from the other. If the duration of the eruption is known, or the time period between collection of two DEMs during an eruption is known, the average volumetric eruption

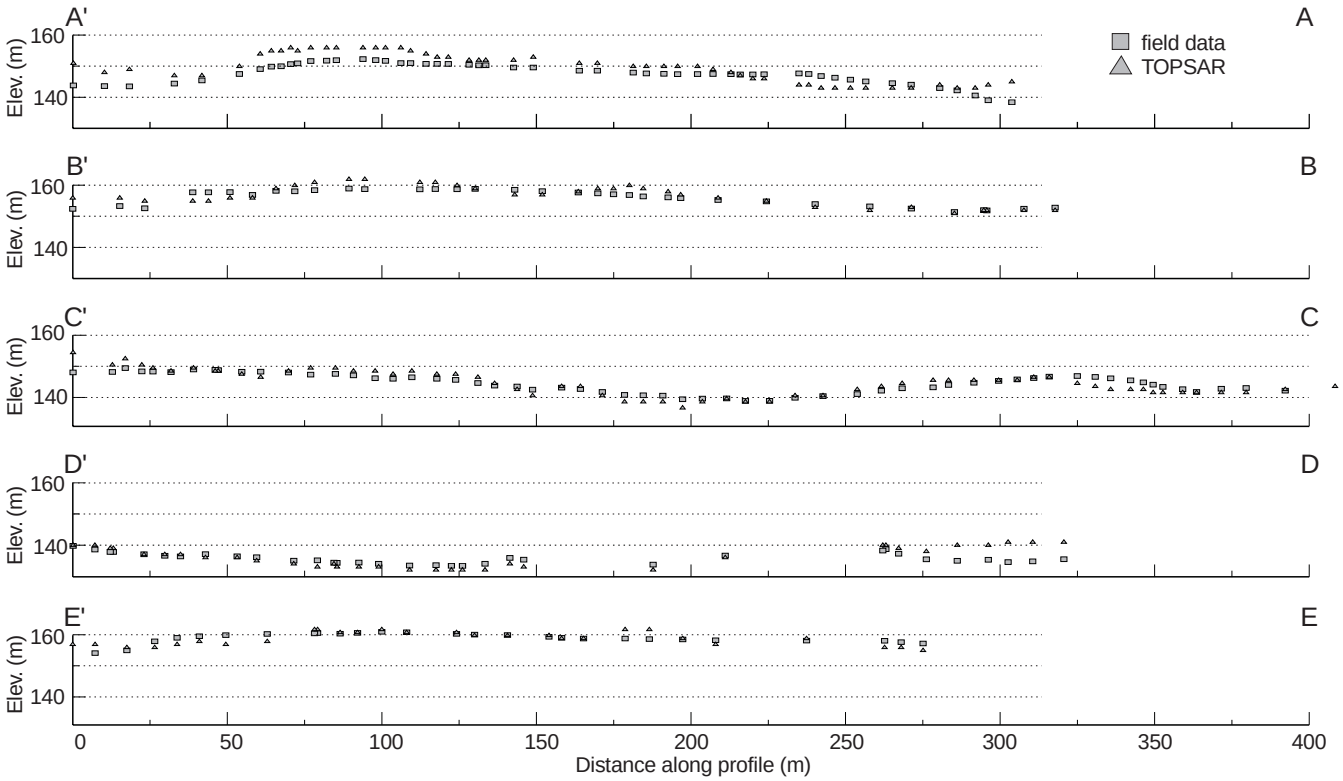


**Fig. 5** Profiles across the 1985 lava flow (no vertical exaggeration). Points correspond to corner-reflector locations (see Fig. 4B). Note the close agreement between data sets

rates can be determined. For meaningful volume results, a critical step is vertically registering the two DEMs to the same pre-eruption datum so that apparent volume is not added or lost due to offsets, tilts, or other effects. In an ideal case simple subtraction of a previous DEM from a present DEM would produce a difference image with values greater than 0 within the area of new volcanic products, and values of zero everywhere else. Integration within the eruption area would yield the volume of new material.

Large areas outside of the current eruption site have positive values in the full-swath difference image that are not removed by the 68-m correction (Figs. 6B and

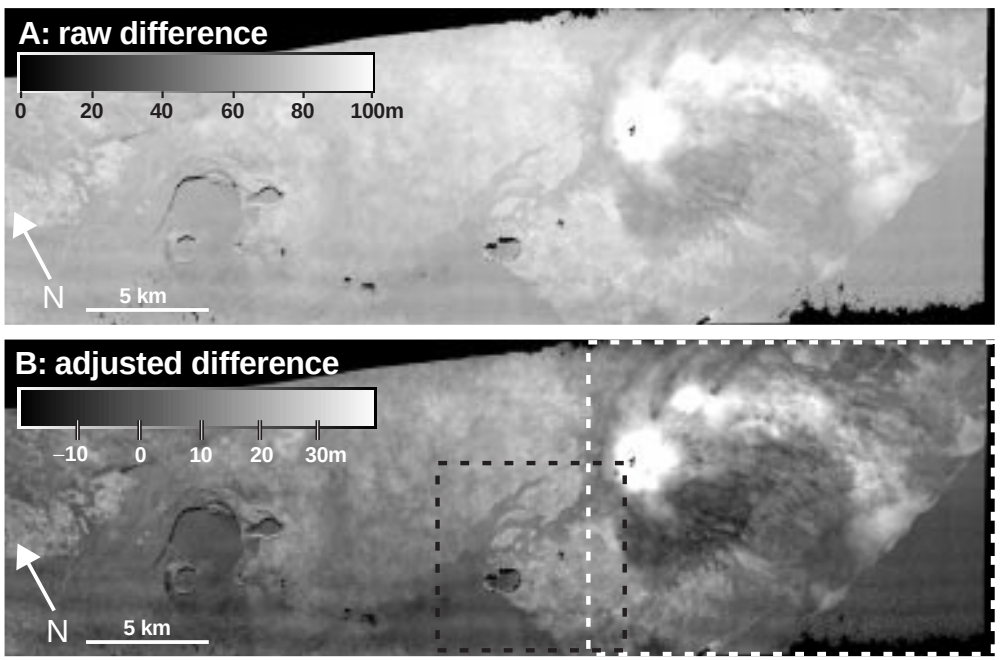


**Fig. 6A, B** Images illustrating vertical adjustment required for comparisons between the TOPSAR and USGS DEMs. **A** Raw difference image of TOPSAR DEM minus USGS DEM. Note that most values are between 60 and 80 m, indicating an overall vertical offset. **B** Adjusted-difference image produced by subtracting 68 m from **A**. Most values are now closer to zero, and the current eruption site stands out more distinctly. *Dashed white box* indicates area of Fig. 2C; *dashed black box* indicates area of Fig. 7

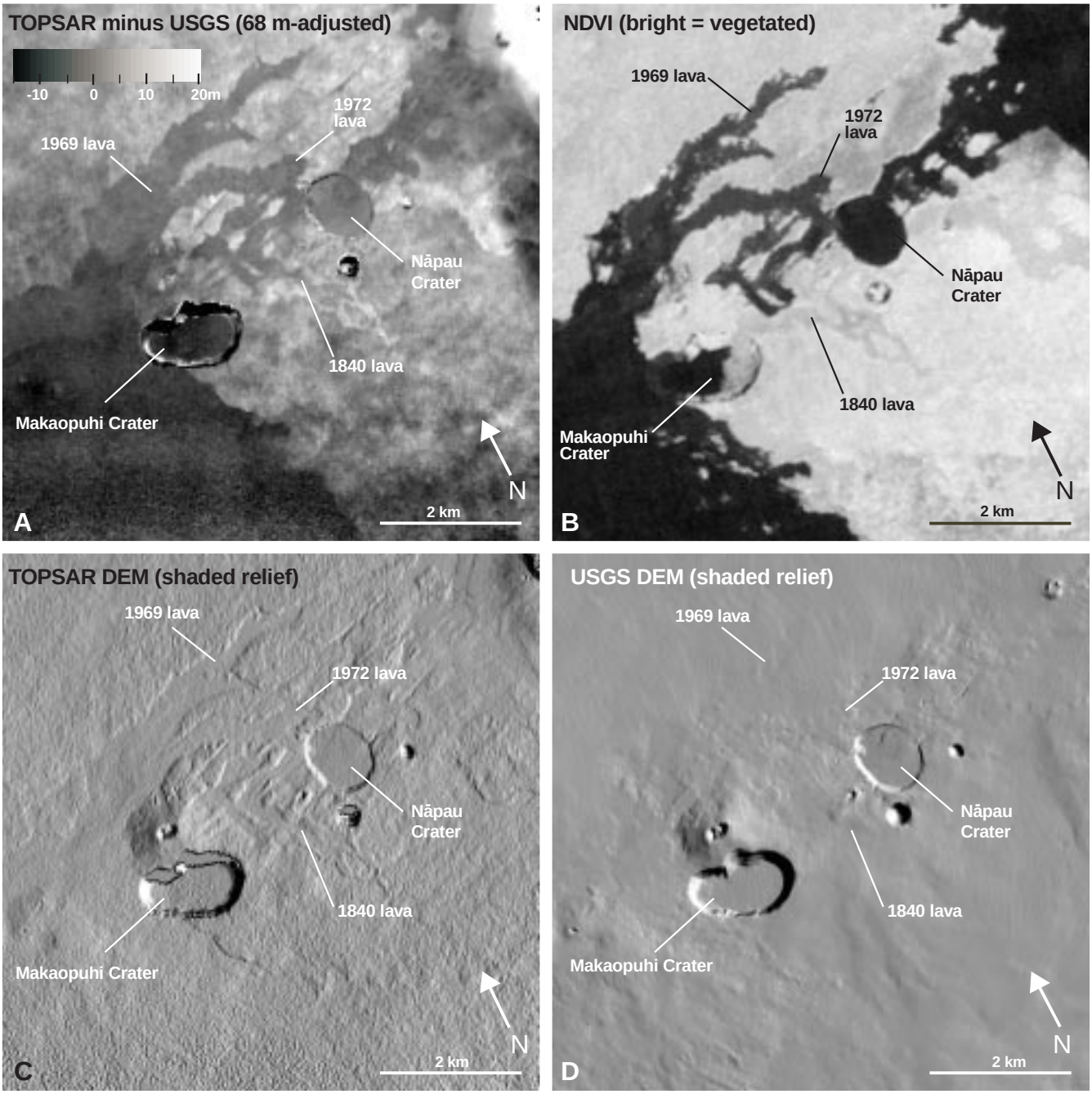


**Fig. 7A–D** Images illustrate vegetation effects on TOPSAR data and thus also on comparisons with USGS data; see Fig. 6B for location. **A** Portion of TOPSAR minus USGS difference image showing flows of 1969 and 1972 (with difference values near zero) surrounded by regions of difference values ranging from +10 to +20 m. **B** NDVI image shows the correspondence between the DEM-difference features in **A** and the boundaries between forest and unvegetated lava flows. **C** The unvegetated flows are lower than the surrounding forest canopy and appear as negative features because TOPSAR cannot penetrate the forest canopy. **D** The USGS data report ground elevations regardless of vegetation cover

7A). This is a region of dense rainforest, which we suspect is causing the TOPSAR elevations to be too high. The normalized difference vegetation index (NDVI; e.g., Asrar 1989) utilizes the ratios between red and near-infrared reflected light to measure plant cover. We produced an NDVI image from bands 3 and 4 of a Landsat TM image collected in October 1991 (Fig. 7B). The features in the difference image correspond closely to vegetated and non-vegetated regions, respectively, in the NDVI data (compare Fig. 7A, B).

This TOPSAR response to vegetation is due to the inability of the C-band radar to penetrate deeply into thick forest. Instead, TOPSAR produces a DEM of some level within the tree canopy that varies depending

on leaf structure and density. One consequence of this is that lava flows that cut through forested regions show up as negative rather than positive features in the TOPSAR data (e.g., the 1969 and 1972 lavas; Fig. 7C). Trees have grown back on the margins of the 1840 flow; thus, the flow margin is a positive feature with respect to the surrounding forest, but the 1840 flow interior (with fewer trees) is a negative topographic feature in the TOPSAR data. The USGS DEM reports ground elevation irrespective of vegetative cover (field checking of canopy heights is used to make corrections to air-photo stereo-grammetry; V. Lukas, pers. commun.). Note that only a small portion of the 1972 flow was thick enough to show up in the USGS data (Fig. 7D).

Using multiple data sets (Fig. 8), we identified control areas that were neither vegetated nor covered by lava flows or vents from the current eruption. The different DEM responses to vegetation would therefore not be a concern, nor would these areas have changed between the times of the two DEMs. These control areas include recent lava flows, sparsely vegetated coastal flows, roads, and clear-cuts. Additionally, careful examination of the TOPSAR DEM indicated that there were narrow regions around the north margin of the new flowfield where the radar was able to penetrate to the pre-eruption surface because the trees had either been knocked over or defoliated; these provided important control in an otherwise heavily vegetated region of the image. Average values in the raw difference image for these control areas fall into two populations (Table 1). Because the seven control areas with the higher average value (75.6 m) constrain a larger portion of the image, we chose that value as a constant offset between the two DEMs, and subtracted it to produce a corrected difference image (Fig. 2C) from which we derived the volumes presented in Table 2.

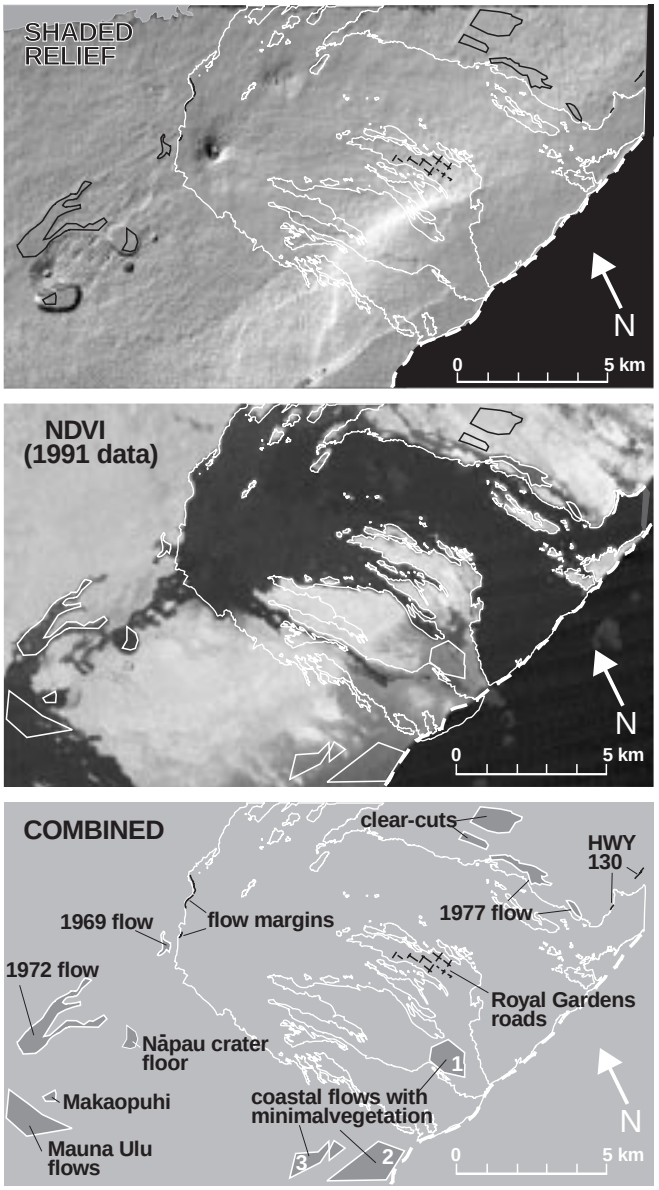


**Fig. 8** Control areas used for vertical registration of the USGS and TOPSAR DEMs prior to volume calculations. Some areas were defined from elevation characteristics (*shaded relief*), some from lack of vegetation (*NDVI*), and others from both. Table 1 compiles statistics for these control areas with regard to the adjusted difference data

## Volume calculations

The current eruption began in January 1983, and summaries of parts of the eruption are in Wolfe et al. (1987, 1988), Heliker and Wright (1991), Mattox et al. (1993), Mangan et al. (1995), and Kauahikaua et al. (1996). The eruption is divided into three major stages over the 1983–1993 time period considered here. The first stage (January 1983 to June 1986) was characterized by 47 eruptive episodes, most of which consisted of 10- to 20-h-long episodes of high fountaining that produced the Pu‘u ‘Ō‘ō cinder cone and numerous overlapping, channelized ‘a‘ā flows. The second major stage was wholly composed of episode 48, which lasted from July 1986 to February 1992 and produced a flow field of tube-fed pāhoehoe lava from the Kūpa‘ianahā satellitic shield. Episode 49 occurred in November 1991 and produced a minor amount of lava. The third major stage, composed of episodes 50–53, started in early 1992 and continued beyond the date of the TOPSAR data (August 1993) until the end of January 1997. This third stage produced a second tube-fed flow field erupted from a satellitic shield built against the uprift and south flanks of Pu‘u ‘Ō‘ō (currently termed the episode 50–53 shield). Episode 55 of the eruption continues at present (February 1999). The careful monitoring, documentation, and volume measurements by the HVO staff provide an excellent data set against which to test the accuracy of the TOPSAR-derived volumes. HVO determined volumes for Pu‘u ‘Ō‘ō lava flows by two independent methods (field-based thickness measurements after, and tilt-based deflation measurements during, each Pu‘u ‘Ō‘ō episode; C. Heliker, pers. commun.).

**Table 1** Statistics for control areas used to adjust difference image for volume calculations

| Control area | No. of pixels | Mean difference (m) | Standard deviation |
|---|---|---|---|
| 1977 flow[a] | 6551 | −2.78 | 1.32 |
| Clear cuts | 12,424 | −6.69 | 2.51 |
| HWY 130[a] | 56 | −2.62 | 1.82 |
| Makaopuhi | 1159 | −11.98 | 2.42 |
| Nāpau Crater[a] | 2352 | +1.77 | 2.12 |
| Royal Gardens roads | 378 | −5.20 | 3.98 |
| North flow margin[a] | 164 | +1.74 | 1.83 |
| Mauna Ulu flows | 14,394 | −10.03 | 2.58 |
| 1972 flow[a] | 17,285 | +1.65 | 1.70 |
| Coastal Area 1 | 10,141 | −8.32 | 2.04 |
| Coastal Area 2 | 18,153 | −6.36 | 3.26 |
| Coastal Area 3[a] | 7877 | −2.09 | 2.93 |
| 1969 flow[a] | 1289 | +1.48 | 1.37 |
| All areas used in 75-m adjustment[a] | 35,574 | 0.00 | 2.84 |
| All areas not used in 75-m adjustment | 56,649 | −7.82 | 3.18 |
| All areas | 92,223 | −4.80 | 4.88 |

**Table 2** Volume comparisons (in $10^6$ $m^3$) between topographic synthetic aperture radar (TOPSAR) and Hawaiian Volcano Observatory (HVO) calculations for products erupted from Kīlauea Volcano, January 1983 to September 1993 (*DRE* – dense rock equivalent)

| Eruptive episode | TOPSAR (raw volume) | TOPSAR (DRE volume) | HVO (DRE volume) | TOPSAR % of HVO volume | TOPSAR % of HVO volume with ocean-entry correction | TOPSAR % of HVO volume with ±2-m error in TOPSAR |
|---|---|---|---|---|---|---|
| Pu‘u ‘Ō‘ō lava | 568 | 426 | | | | |
| Pu‘u ‘Ō‘ō cone | 122 | 61 | | | | |
| Pu‘u ‘Ō‘ō total | 690 | 487 | 392 | 124 | 124 | 96–152 |
| Kūpa‘ianahā lava | 637 | 414 | | | | |
| Kūpa‘ianahā shield | 61 | 25 | | | | |
| Kūpa‘ianahā total | 698 | 439 | 493 | 89 | 159 | 126–191 |
| Episodes 50–53 lava[a] | 120 | 78 | | | | |
| Episodes 50–53 shield[a] | 30 | 12 | | | | |
| Episodes 50–53 total[a] | 150 | 90 | 96 | 94 | 129 | 107–150 |
| Grand total | 1539 | 1016 | 981 | 104 | 138 | 81–125 |

[a]January 1992 to September 1993

Pāhoehoe volumes for Kūpa‘ianahā and episodes 50–53 were determined by HVO from leveling surveys (C. Heliker, pers. comm.) and from very low-frequency electromagnetic induction (VLF) measurements across active lava tubes (Kauahikaua et al. 1996). The VLF-derived volumes have an uncertainty between 5 and 20% and for consistency are calculated to be at the high end of this range (J. Kauahikaua, pers. commun.). The Pāhoehoe volumes determined by HVO include lava eventually emplaced into the ocean (see below).

Raw TOPSAR-derived volumes for the three eruption stages are 690, 698, and $150 \times 10^6$ $m^3$, respectively (Table 2; volumes in areas of overlap were divided evenly between the two stages). These are bulk volumes that include vesicles, lava tubes, spaces between clinkers, etc., whereas the volume data reported by HVO have been converted to dense rock equivalent (DRE). We converted the bulk TOPSAR volumes to DRE using the following constraints: Wolfe et al. (1987) suggest a void correction of 25% for ‘a‘ā flows so we multiplied the TOPSAR-derived ‘a‘ā volumes by 0.75. Pu‘u ‘Ō‘ō consists of pyroclastic material having a large range in vesicularity, from reticulite with >95% vesicles to scoria with ~75% vesicles (Mangan and Cashman 1996). However, much of Pu‘u ‘Ō‘ō also consists of rheomorphic lava produced when pyroclastic material accumulated rapidly enough to form spatter-fed flows. The rheomorphic lava tends to have a low vesicularity, and we therefore used an overall void space correction of 0.5 for Pu‘u ‘Ō‘ō. Pāhoehoe collected at the episode 50–55 vent had a vesicularity ranging between 50 and 88% (average = 69%; Cashman et al. 1994). This would suggest multiplying the TOPSAR-derived volumes of the Kūpa‘ianahā and episode 50–55 shields by 0.31; however, we multiplied them by 0.4 to take into account some compaction due to the collapse of shelly pāhoehoe flow units. The average vesicularity of tube-fed pāhoehoe away from the shields measured

by Cashman et al. (1994) was 35%, so we multiplied the TOPSAR-derived volumes by 0.65. These void-space corrections produce TOPSAR-derived DRE volumes of 487, 438, and $90 \times 10^6$ m$^3$ for the three stages, which are 124, 89, and 94% of the HVO-derived volumes, respectively (Table 2).

None of the Pu'u 'Ō'ō lava entered the ocean, and only a small amount is outside the TOPSAR swath. The relatively good agreement between the TOPSAR-derived Pu'u 'Ō'ō volume and that measured by HVO is thus encouraging. An important consideration is that lava was emplaced offshore during both the Kūpa'ianahā and episode 50–53 stages of the eruption and is therefore not accounted for in the TOPSAR measurement. Compilation of descriptions in HVO monthly reports indicates that approximately 44 and 27% of the lava entered the ocean during the Kūpa'ianahā and episode 50–53 stages, respectively. Adding these percentages to the TOPSAR volumes produces values that are 159 and 129% of the HVO values (Table 2).

Dividing the TOPSAR-derived volumes by the durations of each eruption stage allows us to calculate volumetric effusion rates. For the Pu'u 'Ō'ō/Kūpa'ianahā and episode 50–53 stages these are 4.5, 4.5, and 2.7 m$^3$/s, respectively (accounting for both void space and emplacement offshore). These compare to volumetric effusion rates from the HVO data of 3.6, 2.8, and 2.1 m$^3$/s, respectively. Additionally, we determined that the Pu'u 'Ō'ō cinder cone comprises 12% of the DRE volume erupted during that eruption stage. For the Kūpa'ianahā and episodes 50–53 stages, the satellitic shields comprise 6 and 13% of the subaerially erupted products, respectively.

We suspect that there are four reasons why the TOPSAR-derived volumes are higher than those measured by HVO. Firstly, the average vesicularities on which the bulk volume to DRE are based may be too generalized for application to an entire flow field. Secondly, the correction for lava that entered the ocean has large uncertainties. These volumes are considerable (Table 2) and are based on estimates that in the field are often difficult to make and thus difficult to quantify from the written reports. Thirdly, although we have corrected for vesicularity, we have not accounted for empty lava tubes, drained toes, gas blisters, or spaces between flow units. Rough calculations (Appendix 2), however, indicate that these voids amount to $<5\%$ of the flow field and are thus probably not a significant contributor to the TOPSAR–USGS volume discrepancy. Fourth and finally, there may be tilts or warps in either the TOPSAR or USGS DEMs, although none are apparent. Such warps might explain the area of negative difference south of Pu'u 'Ō'ō (Figs. 2C, 6), which, if anything, should show a positive difference because it is heavily vegetated. We note that previous use by us of a different pre-eruption USGS DEM required considerable effort to remove tilts and offsets.

Our field studies show agreement between TOPSAR and TFS data to within 1–2 m on both pāhoehoe and flows (Figs. 2, 5). Adding or subtracting 1–2 m of lava over the areas of the three eruption stages gives uncertainties of $\pm$11–22, 10–20, and 8–17% of the calculated TOPSAR volumes for the three eruption stages, respectively, and corresponds to a range between 81 and 125% of the total USGS-derived volumes (Table 2). We note, however, that at the field sites the TOPSAR data are consistently neither high nor low with respect to the TFS measurements, and we expect that corresponding variations in calculated volume will cancel each other out rather than add or subtract significantly.

A previous attempt to use these same TOPSAR data for calculation of erupted products was made by Johnson et al. (1996). They obtained a total volume of $1600 \times 10^6$ m$^3$, almost twice the HVO value. The details of their method were not presented, however, so it is not possible to understand the volume discrepancy.

## Conclusions and future studies

We conclude that TOPSAR data are useful both for the morphological and volumetric characterization of individual volcanic features such as faults, lava flows, and cinder cones, as well as for large-scale flow fields. Field work indicates that in areas of sparse vegetation (e.g., caldera or recent flows), TOPSAR elevations are accurate to within 1–2 m on both smooth and rough surfaces. Calculations based on topographic profiles or morphologies derived from TOPSAR are therefore highly accurate. Additionally, the estimation of eruption volume and volumetric effusion rates for the ongoing activity at Kīlauea demonstrates that high-quality digital elevation data, such as TOPSAR, can be used to quantify volcanic processes.

Various features visible in the difference image contain information about the ongoing eruption. Features in the image related to burial by erupted products include Pu'u Kamoamoa and an unnamed cinder cone west and south–southeast, respectively, of Pu'u 'Ō'ō, and a large earth crack between Pu'u 'Ō'ō and Kūpa'ianahā. Additionally, thickness variations within the flow field may yield information about the emplacement of a long-lived tube-fed flowfield. A detailed examination of these features is ongoing.

In addition to studying lava flows, the same technique presented here could, at other volcanic locations, be used to characterize the volume changes of cinder cones, pit craters, pyroclastic flows, and lahars, depending on their thickness. Where multiple TOPSAR DEMs have been collected over a period of years, or the TOPSAR data set can be compared with DEMs derived from the Space Shuttle (SIR-C) radar data collected in 1994 or the upcoming Shuttle Radar Topography Radar Mission (SRTM), time series investigations of erosion, subsidence, inflation, or construction on a volcano can be undertaken (MacKay et al. 1998). These conclusions should encourage additional volcanological

utilization of TOPSAR data, particularly due to the amount of time required to calculate volumes by field techniques or the inability to physically visit particular volcanic sites.

We caution that these DEM data required significant image processing resources as well as ancillary data (e.g., the Landsat TM scene) before useful geological information could be extracted. Most of the orientation and offset corrections are not required when using TOPSAR data collected after 1995, because superior navigational data are now collected as part of the TOPSAR metadata. However, because topographic-change studies will almost certainly involve comparison between interferometric and photogrammetric DEMs, vegetation corrections, perhaps requiring complex adjustments, may still be required to achieve accurate results. L-band TOPSAR data are now also collected, and the ability of L-band to penetrate farther into vegetation (Imhoff et al. 1986) may make this less of an issue. The upcoming flight of the Vegetation Canopy Lidar space mission in 2000 will have the ability to recover surface topography beneath a vegetation canopy, allowing vegetation responses in TOPSAR data to be assessed.

We encourage readers to explore the utility of the TOPSAR data sets for volcano studies. The Jet Propulsion Laboratory maintains a World Wide Web site that allows the TOPSAR data base to be searched and quick-look products to be viewed and ordered. The address for this site is: http://airsar.jpl.nasa.gov/data/data.html

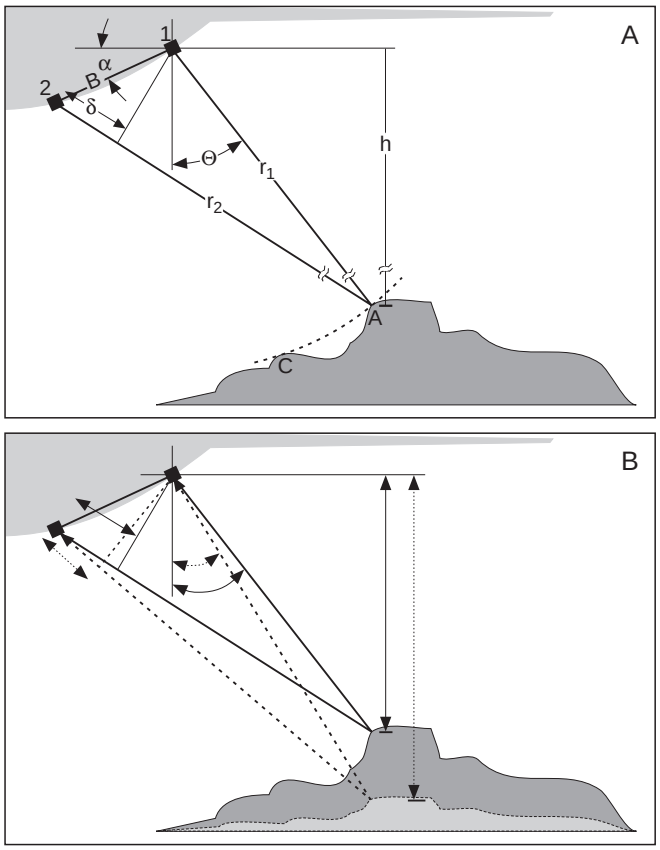


**Fig. A1** The geometry of a radar system used to collect topography interferometrically

## Appendix 1: The geometry of interferometric radar

Figure A1A presents the geometry of an interferometric radar system and how it determines the vertical component (h) of the distance between the aircraft and the surface at point A, which in combination with the known altitude of the aircraft yields elevation. In Fig. A1B two surfaces (solid and dashed) are shown to illustrate how the measured parameters vary with topography.

In Fig. A1A the two antennae, labeled 1 and 2, are separated by a baseline B. This baseline has a fixed length, which on TOPSAR is 2.6 m, and is at an angle $\alpha$ with respect to the horizontal plane. The diagram indicates the return signals received from point A at antennae 1 and 2; the outgoing signal (sent by only one antenna) is not shown. The signal received at antenna 1 has traveled a distance $r_1$ from point A, and that at antenna 2 a distance $r_2$, which is equal to $r_1$ plus a differential distance $\delta$.

To determine topography we need to determine h and $\phi$ (the angle between $r_1$ and vertical) for each pixel. However, because the outgoing signal is an $\sim 60°$-wide beam, it is not possible to do so with only one antenna; note that point C has the same value of $r_1$ as point A, but a different value of $\phi$. In fact, with only a single antenna, points C and A would be indistinguishable (the condition known as layover). Layover is a common problem affecting steep slopes in radar scenes. It occurs when a higher point on a feature is physically at the same distance from (or closer to) the radar antenna compared with lower points on the feature, even though in a map view the top is farther away. This causes the return signal from the top of the feature to arrive at the antenna at the same time as (or before) the return signal from the base, and the information from the two is combined in a way that cannot be rectified for position or height.

The interferometric technique allows the determination of $\phi$ and in turn h for each point within the radar scene. Combined with flight parameters these produce topography. The cosine rule gives:

$$r_2^2 = r_1^2 + B^2 - 2r_1 B \sin(\phi-\alpha). \quad \text{(A1)}$$

This can be rearranged to yield:

$$\sin(\phi-\alpha) = (r_2^2 - r_1^2 - B^2)(-2r_1B)^{-1} \quad \text{(A2)}$$

and then:

$$\phi = \alpha + \sin^{-1}[(r_2^2 - r_1^2 - B^2)(-2r_1B)^{-1}] \quad \text{(A3)}$$

Parameters of the radar system result in uncertainties for $r_1$ and $r_2$ of $\pm 3.75$ m (Zebker et al. 1992), which

would be significant if they were both in the formula. However, note from Fig. A1 that $r_2 = r_1 + \delta$. $\delta$ can be measured very precisely in terms of the phase difference between the signals received at $r_1$ and $r_2$ (this is the interferometry part of the process). Substituting $r_1 + \delta$ for $r_2$ into Eq. (A3) produces a result that, although not very compact, yields $\phi$ in terms of the known or measured quantities B, $\alpha$, $\delta$, and $r_1$. Once $\phi$ is determined (for each pixel), trigonometry yields h.

In reality $\delta << B << r_1$ and $r_2$, and in fact $r_1$ and $r_2$ are assumed to be parallel to simplify the derivation. Additionally, the interferometric technique differs significantly from radar stereo, in which the angle between the equivalents of $r_1$ and $r_2$ is calculated.

## Appendix 2: Non-vesicle void space

Maps and descriptions in Realmuto et al. (1992) and Mattox et al. (1993) indicate that perhaps ten major lava tubes developed as far as the coastal plain within the flow field and thus have the potential to have drained out to leave void space. Using an average tube radius of 2 m and an average tube length of 12 km from Kūpa'ianahā to the landward edge of the coastal plain (beyond which draining out is unlikely; Hon et al. 1994) produces a total drained-out tube volume of $\sim 1.5 \times 10^6$ m$^3$. This is $\sim 0.4\%$ of the TOPSAR-derived DRE volume for (Table 2) and thus is not an explanation for the TOPSAR–USGS discrepancy.

G.J. Taylor (pers. commun.) measured cross-sectional areas of flow units within a tube-fed flow exposed in a roadcut along the Chain of Craters Rd. His data show that the void space of drained flow units and gas blisters comprises $\sim 3\%$ of the flow field (assuming void volume equals void area in cross section), again not sufficient to account for the TOPSAR–USGS volume discrepancy.

**Acknowledgements** This paper is dedicated to the memory of retired HVO Chief of Operations, Reggie Okamura. The data presented here were processed at the Jet Propulsion Laboratory and were kindly provided by H. Zebker and E. O'Leary. We are indebted to J. Kauahikaua for very useful discussions and for making us aware of, and initially providing, the 10-m USGS DEM. We thank D. Thomas, D. Bevens, J. Anderson, and C. Johnson of the Center for the Study of Active Volcanoes (University of Hawai'i at Hilo) for use of the total field station, K. Yamashita and C. Johnson for instructions on its use, and our field assistants D. Ford, J. Johnson, and J. Babb. Helpful reviews were provided by A. Harris and N. Stevens, and formal reviews by J. Plaut, D. Swanson, and the staff of HVO improved the manuscript significantly. This research was funded by NASA grant no. NAG 5-3000, to P. Mouginis-Mark under the Digital Topography Program. This is HIGP Publication no. 1042, and SOEST Contribution no. 4784.

## References

Asrar G (1989) Theory and applications of optical remote sensing. Wiley, New York

Cashman KV, Mangan MT, Newman S (1994) Surface degassing and modifications to vesicle size distributions in active basalt flows. J Volcanol Geotherm Res 61:45–68

Crisp JA (1984) Rates of magma emplacement and volcanic output. J Volcanol Geotherm Res 20:177–201

Dvorak JJ, Dzurisin D (1993) Variations in magma supply rate at Kilauea Volcano, Hawaii. J Geophys Res 98:255–268

Elachi C (1988). Spaceborne radar remote sensing: applications and techniques. IEEE Press, New York

Evans DL, Farr TG, Zebker HA, van Zyl JJ, Mouginis-Mark PJ (1992) Radar interferometry studies of the Earth's topography. EOS 73:553–558

Fink JH, Zimbelman J (1990) Longitudinal variations in rheological properties of lavas: Puu Oo basalt flows, Kilauea Volcano, Hawaii. In: Fink JH (ed) Lava flows and domes: emplacement mechanisms and hazard implication. Springer, Berlin, pp 157–173

Gabriel AK, Goldstein RM, Zebker HA (1989) Mapping small elevation changes over large areas: differential radar interferometry. J Geophys Res 94:9183–9191

Heliker C, Wright TL (1991) The Puu O'o–Kupaianaha eruption of Kilauea. EOS 72:521–530

Holcomb RT (1987) Eruptive history and long-term behavior of Kilauea Volcano. US Geol Surv Prof Pap 1350:261–350

Hon K, Kauahikaua J, Denlinger R, Mackay K (1994) Emplacement and inflation of pahoehoe sheet flows: observations and measurements of active lava flows on Kilauea Volcano, Hawaii. Geol Soc Am Bull 106:351–370

Hulme G (1974) The interpretation of lava flow morphology. Geophys J R Astron Soc 39:361–383

Imhoff M, Story M, Vermillion C, Khan F, Polcyn F (1986) Forest canopy characterization and vegetation penetration assessment with space-borne radar. IEEE Trans Geosci Remote Sens 24:535–542

Izenberg, NR, Arvidson RE, Brackett RA, Saatchi SS, Osburn GR, Dohrenwend J (1996) Erosional and depositional patterns associated with the 1993 Missouri River floods inferred from SIR-C and TOPSAR radar data. J Geophys Res 101:149–167

Johnson J, Klemperer S, Zebker H (1996). Measuring lava flow output from Hawaii's east rift. Earth Observ Mag 5:16–22

Kauahikaua J, Mangan M, Heliker C, Mattox T (1996) A quantitative look at the demise of a basaltic vent: the death of Kupaianaha, Kilauea Volcano, Hawaii. Bull Volcanol 57:641–648

Lin Q, Vesecky JF, Zebker HA (1994). Comparison of elevation derived from INSAR data with DEM over large relief terrain. Int J Remote Sens 15:1775–1790

MacKay ME, Rowland SK, Mouginis-Mark PJ, Garbeil H (1998) Thick lava flows of Karisimbi Volcano, Rwanda: insights from SIR-C interferometric topography. Bull Volcanol 60:239–251

Madsen SN, Martin JM, Zebker HA (1995) Analysis and evaluation of the NASA/JPL TOPSAR across-track interferometric SAR system. IEEE Trans Geosci Remote Sens 33:383–391

Mangan MT, Cashman KV (1996) The structure of basaltic scoria and reticulite and inferences for vesiculation, foam formation, and fragmentation in lava fountains. J Volcanol Geotherm Res 73:1–18

Mangan MT, Heliker CC, Mattox TN, Kauahikaua JP, Helz RT (1995) Episode 49 of the Pu'u 'O'o-Kupaianaha eruption of Kilauea Volcano: breakdown of a steady-state eruption era. Bull Volcanol 57:127–135

Massonnet D, Rossi M, Carmona C, Adragna F, Peltzer G, Feigl K, Rabaute T (1993) The displacement field of the Landers earthquake mapped by radar interferometry. Nature 364:138–142

Mattox TN, Heliker C, Kauahikaua J, Hon K (1993) Development of the 1990 Kalapana flow field Kilauea Volcano, Hawaii. Bull Volcanol 55:407–413

Moore JG, Mark RK (1992) Morphology of the Island of Hawaii. Geol Soc Am Today 2:257–262

Mouginis-Mark PJ, Garbeil H (1993) Digital topography of volcanoes from radar interferometry: an example from Mt. Vesuvius, Italy. Bull Volcanol 55:566–570

Mouginis-Mark PJ, Rowland SK, Garbeil H (1996) Slopes of Western Galapagos volcanoes from airborne interferometric Radar. Geophys Res Lett 23:3767–3770

Realmuto VJ, Hon K, Kahle AB, Abbot EA, Pieri DC (1992) Multispectral thermal infrared mapping of the 1 October 1988 Kupaianaha flow field, Kilauea volcano, Hawaii. Bull Volcanol 55:33–44

Rowland SK (1996) Slopes, lava flow volumes, and vent distributions on Volcán Fernandina, Galápagos Islands. J Geophys Res 101:657–672

Stevens NF, Murray JB, Wadge G (1997) The volume and shape of the 1991–1993 lava flow field at Mount Etna, Sicily. Bull Volcanol 58:449–454

USGS (1990) Digital Elevation Models Data Users Guide 5:51 pp

Wadge G (1977) The storage and release of magma on Mount Etna. J Volcanol Geotherm Res 2:361–384

Wessel P, Smith WHF (1995) New version of the Generic Mapping Tools Released. EOS Trans AGU 76:329

Wolfe EW, Garcia MO, Jackson DB, Koyanagi RY, Neal CA, Okamura AT (1987) The Puu Oo eruption of Kilauea Volcano, episodes 1–20, January 3, 1983, to June 8, 1984. US Geol Surv Prof Pap 1350:471–508

Wolfe EW, Neal CA, Banks NG, Duggan TJ (1988) Geologic observations and chronology of eruptive events. US Geol Surv Prof Pap 1463:1–97

Zebker HA, Goldstein R (1986) Topographic mapping from interferometric SAR observations. J Geophys Res 91:4993–4999

Zebker HA, Madsen SN, Martin J, Wheeler KB, Miller T, Lou Y, Alberti G, Vetrella S, Cucci A (1992) The TOPSAR interferometric radar topographic mapping instrument. IEEE Trans Geosci Remote Sens 30:933–940

Zebker HA, Werner CL, Rosen PA, Hensley S (1994a) Accuracy of topographic maps derived from ERS Interferometric radar. IEEE Trans Geosci Remote Sens 32:823–836

Zebker HA, Farr TG, Salazar RP, Dixon TH (1994b) Mapping the world's topography using radar interferometry: the TOPSAT mission. Proc IEEE 82:1744–1786